Science
AAAS

Supplementary Materials for

A high-temperature nanostructured Cu-Ta-Li alloy with complexion-stabilized precipitates

B. C. Hornbuckle *et al*.

Corresponding authors: M. P. Harmer, mph2@lehigh.edu; K. Solanki, kiran.solanki@asu.edu; K. A. Darling, kristopher.a.darling.civ@army.mil

Science **387**, 1413 (2025)
DOI: 10.1126/science.adr0299

The PDF file includes:

Materials and Methods

High Energy Mechanical Alloying

Nanocrystalline Cu-3Ta at.% and Cu-3Ta-0.5Li at.% powders were mechanically alloyed through high-energy cryogenic ball milling. A hardened steel vial was filled with the appropriate quantity of Cu, Ta, and LiH powders obtained from Alfa Aesar to yield 10 grams of alloyed powder. A ball-to-powder weight ratio of 5:1 with 440C stainless steel ball bearings was loaded into the vial under an argon atmosphere with less than 1 ppm levels of oxygen and H_2O prior to milling. High-energy cryogenic ball milling was conducted using a SPEX 8000M shaker mill with a modified nylon sleeve attachment. This nylon sleeve maintains the three-dimensional milling kinetics while enabling the continuous flow of liquid nitrogen around the sealed milling vial. To ensure the milling vial reached the desired cryogenic temperature (-196˚C), liquid nitrogen was flowed for 20 minutes prior to starting the milling process. Once started, the powder was milled continuously for 4 hours.

Powder with a particulate size range of 20-100 μm was collected with a yield greater than 99%. Compacts having a diameter of 3 mm were made by uniaxial pressing the as-milled powder in a tungsten carbide die at 3.0 GPa. The green compacts were annealed in an atmosphere of Ar-H_2 forming gas over a range of temperatures from 400°C to 1050°C (97% T_M) for 1 hour. To further test the long-term, elevated temperature stability of the two compositions, additional heat treatments were performed for 10,000 hours over the same temperature range. The compacts were then prepared for hardness measurements and initial microstructural characterization by polishing to at least a 1 μm final polishing step. Vickers microhardness tests were performed on each annealed alloy condition using a Buehler's Tukon 1202 hardness indenter with a Vickers diamond indenter using a 100 g load and a dwell time of 10 s. The reported hardness is the average of 10 indents on each sample with the error bars representing the standard deviation.

Samples for mechanical testing were consolidated to bulk using equal channel angular extrusion (ECAE). For this process, the as-milled powder was placed in nickel cans and sealed inside a glove box under Argon atmosphere. The die assembly used for processing the billets was preheated to 623 K (350 °C) to minimize thermal loss during the ECAE process. The billets, heated and equilibrated to 973 K (700 °C) for 40 min, were quickly dropped into the ECAE tooling and extruded at a rate of 25.5 mm/s, following route B_c to avoid imparting a texture to the consolidated powder. This process was repeated four times, resulting in an equivalent strain of ~4.6.

Transmission Electron Microscopy

Thin specimens for transmission electron microscopy (TEM) and aberration-corrected scanning transmission electron microscopy (ac-STEM) were prepared using in-situ lift-out methods with either an FEI Scios or FEI Helios focused ion beam instrument. ac-STEM was performed using a JEOL ARM-200CF fitted with a JEOL Centurio 100 mm^2 silicon drift detector used for energy dispersive spectroscopy (EDS). TEM was conducted using a JEOL 2100F transmission electron microscope. Thin specimens for ac-STEM were also ion milled using a Fischione 1040 NanoMill instrument to remove Ga ion beam damage resulting from the thinning process.

Atom Probe Tomography

Atom probe tomography (APT) tips were prepared using in-situ lift-out methods with an FEI Helios focused ion beam instrument. APT was performed using a Cameca Local Electrode Atom Probe (LEAP) 5000XR system operated in laser mode at 50K, pulse energy of 50 pJ, auto pulse rate control enabled with a minimum mass spectrum range of 300 Dalton, and a detection rate of 0.5%. The data were reconstructed using the Cameca IVAS version 3.8.4 platform.

The specific parameters used in generating the various atom probe figures both within the manuscript and the supplemental will be described below. For Figure S10, atom maps of Cu and TaO, and a Li isoconcentration surface set to 0.5 at.% Li for the ternary alloys as shown in the first row of Figure S10 (Fig. S10A-E). Similar maps, but excluding Li, were constructed for the optimized Cu-3Ta alloy binary cluster chemistry (Fig. S11). Density contour plots of Cu, Li, and TaO representing two-dimensional (2D) slices taken along the z-direction of the atom probe tip can also be seen in Figure S10 (Figure S10F-I). For Figure 2 in the main manuscript, parts A and C utilize 1 at.% Li isoconcentration surface. An example of the full mass spectrum and integration windows used for atom maps is shown in Fig. S12.

Simulation Techniques

The stability of the Cu_3Li precipitate in the Cu matrix was explained by highlighting the role of Ta in stabilizing the $L1_2$ precipitate. TEM images along the [110] zone axis show the presence of a bilayer of Ta around the $L1_2$ Cu_3Li phase. Density functional theory using the Vienna ab-initio simulation package was employed to observe the energetics of precipitate formation. Plane-wave basis sets and periodic boundary conditions were used together with the generalized gradient approximation (GGA) within the Perdew-Burke-Ernzerhof (PBE) exchange-correlation functional. The plane wave cutoff is chosen to be 500 eV to ensure convergence and total energy convergence criteria of 10^{-3} eV for self-consistency in all calculations. Surface energies were calculated after adding a vacuum to test for convergence of choice of k-points. A single gamma-

centered k-point grid is chosen due to the large size of the supercell and in order to minimize contributions from periodic interactions. A vacuum region of approximately 15 Å was applied in the direction perpendicular to the interface plane to avoid nearest-neighbor interactions from adjacent interface structures. The quasi-Newtonian method was employed to relax the ions to their instantaneous ground states. The final relaxed structure is shown in Fig 10C. The electronic occupations treated in the functionals for Li, Cu, and Ta are $1s^2 2s^1$, $[Ar]\ 3d^{10} 4s^1$, $[Xe]\ 4f^{14} 5d^4 6s^1$ with 1, 11, and 5 valence electrons respectively. Note that the possible locations, which are occupied by Ta, are only substitutional sites because of the atomic radii of Cu and Ta. Hence atoms at the boundary of Cu_3Li are replaced with Ta in order to model the bilayer of Ta observed in TEM images around the Cu_3Li precipitate giving an interplanar Ta spacing of ~1.6Å confirming observations from STEM imaging. Further, the interface model consisted of 4 layers of Cu with 4 layers of Cu_3Li, and the Cu:Li ratio was exactly 3:1 in the top Cu_3Li slab to preserve stoichiometry. This resulted in a large supercell with a total of 459 atoms size of the simulation block is comparable to the observed nano-cluster in TEM images. Since Ta addition is done substitutionally, the number of atoms is the same in the supercell with and without Ta.

For the supercell models as shown in Fig 10E, the Cu (110)/Cu_3Li (110) interface was made by choosing the [110] direction of Cu_3Li and aligning with [110] of the Cu matrix. The green, yellow, and orange spheres correspond to Li, Ta, and Cu atoms, respectively. The total average misfit was calculated using the Bramfitt two-dimensional misfit method using the following equation:

$$\delta_{(hkl)_{Cu_3Li}}^{(hkl)_{Cu}} = \sum_{i=1}^{3} \left[\left(\left| d_{[uvw]_{Cu}}^{i} \cos\Delta\theta - d_{[uvw]_{Cu_3Li}}^{i} \right| / d_{[uvw]_{Cu_3Li}}^{i} \right) / 3 \right] \times 100\% \quad (1)$$

This calculates the average strain as well as accounts for the misorientation, where $(hkl)_{Cu_3Li}$ and $(hkl)_{Cu}$ are the low index lattice planes of the $L1_2$ phase and the matrix respectively; $[uvw]_{Cu_3Li}$ and $[uvw]_{Cu}$ are the low-index crystal orientations in $(hkl)_{Cu_3Li}$ and $(hkl)_{Cu}$; and $d_{[uvw]_{Cu_3Li}}$and $d_{[uvw]_{Cu}}$are the interatomic spacing along $[uvw]_{Cu_3Li}$ and $[uvw]_{Cu}$; $\Delta\theta$ is the angle between $[uvw]_{Cu_3Li}$ and $[uvw]_{Cu}$.

The Cu_3Li exhibits $L1_2$ structure at low temperatures, however at a sufficiently high temperature, it can lose the $L1_2$ ordering. Thus, the quasi-harmonic approximation was employed using a phonopy package to calculate the phonon density of states and entropy as a function of temperature. The special quasi-random structures were generated to replicate the disordered state using the ATAT toolkit. For the phonon calculations, supercell and finite displacement approaches were used with a $3 \times 3 \times 3$ supercell of the conventional unit cell (108 atoms) and atomic displacements of 0.01 Å.

$$E_{o-d} = (E_{L12} - E_{disordered})/N \quad (2)$$

Configurational contribution to the entropy of a random binary solution was calculated using the following,

$$\Delta S_{mix} = -k_B(x\ ln(x) + (1-x)\ ln(1-x)) \quad (3)$$

The vibrational contribution was calculated as a function of temperature using phonopy, and the total entropy was calculated by adding both terms of entropy. Finally, using

$$\Delta G = \Delta H - T\Delta S$$
$$Cu_3Li(ordered) \xrightarrow{\Delta G} Cu_3Li(disordered) \quad (4)$$

Setting $\Delta G = 0$ at the order-disorder transition and using the difference in energy for ordered and disordered structures obtained by DFT calculations.

In order to obtain the interface strength of the bilayer Ta substituted $L1_2$ Cu_3Li precipitate with the Cu lattice, the ideal work of separation (W), which is a direct measure of the interface bond strength and is defined as the amount of reversible work done in the separation of a single interface into two free surfaces. It is understood that the higher the work of separation more stable the interface structure, and it is more difficult to separate the two slabs forming the interface mechanically. Since there are very few experimental techniques that directly measure the work of separation, these values obtained computationally are idealistic and should only be treated as a comparative measure between similarly structured interfaces. In actual experiments, the work of separation can be lower because of the presence of surface layers (such as oxides and nitrides) and other experimental phenomena occurring upon trying to separate the two interfaces, making it challenging to obtain the exact values that would be desirable. We define the methodology of calculating the work of separation using the following equation (Table S2)

$$W = \frac{E_1 + E_2 - E_{12}}{A} \quad (5)$$

In the above equation E_1, E_2, E_{12} represent the total energy of a slab of Cu_3Li (with or without Ta as bilayer) with vacuum, a slab of pure Cu with vacuum, and the total energy of a slab with a combined interface between the $L1_2$ Cu_3Li phase (with or without Ta) with pure Cu. The area of the interface is given by A. Interface energy gives a degree of how stable the bonds are present in the interface as compared to bonding in the bulk regions. The lower the interface energy is the more stable the interface. The interface energy relates to the ideal work of separation as follows (Table S2)

$$\gamma = \sigma_1 + \sigma_2 - W \quad (6)$$

Here, γ is the interface energy between two slabs, which in this case the Cu_3Li (with or without Ta bilayer) on one side and pure Cu with orientations as observed in STEM imaging. Surface energies (σ_1, σ_2) were calculated for both slabs under consideration using the following formulation as shown below

$$\sigma_i = \frac{E_i - \sum_j N_j \mu_j}{2A}$$

Here E_i is the total energy of slabs as mentioned previously, while the summation with subscript j represents the chemical species. N_j represents the number of atoms in species j, and μ_j is the chemical potential of the species j. Here the species are of Cu, and Li, and in the structure with a bilayer of Ta, all three Cu, Li, and Ta are denoted within the j subscript. The factor of 2 arises because there are two surfaces created when a vacuum is added in the z-direction one at the top and one at the bottom. It is made sure that both terminating surfaces of the slabs have the same surface terminations so that σ_i represents the same surface and not an average of two different terminating surfaces.

The Valence charge transfer plots were calculated with an iso-surface value of 0.0025 e/Å^3 using the charge density difference in the converged charge densities of the interface, and individual slabs according to the following equation.

$$\Delta\rho = \rho_{AB} - \rho_A - \rho_B \quad (7)$$

The Bader charge difference is calculated using: $Bader\ Charge\ difference = ZVAL - Bader\ charge\ on\ atom$, where ZVAL is the initial number of valence electrons present from the VASP potential file used, and Bader charge on the atom is the total Bader charge present in the Bader volume around that atom in the final structure.

To understand the effects of Ta addition, Density of States (DOS) calculations were performed. The DOS curve describes the number of states available to be occupied per interval of energy at each energy level. Local DOS describes the distribution of the electronic states in the local region of a volume around the core of atoms.

Mechanical characterization at quasi-static and creep conditions

Compression quasi-static experiments were conducted to characterize the high temperature behavior of nanocrystalline Cu-Ta-Li alloys. An Instron load frame equipped with a 50 kN load cell and a high temperature clamshell furnace capable of a maximum temperature of 1200° C was utilized to perform the experiments. Further, MAR-M (Ni alloy) rods were used with WC (tungsten carbide) platens to avoid any deformation in the setup at high temperatures. Tests were performed on ECAE-processed cylindrical samples of diameter and height of 3 mm each at a strain rate of

0.001 s^{-1} with testing temperatures varied from 298 K – 873 K. A soak time of 30 minutes was used at each temperature before testing. Yield strength was measured at 0.2% strain and plotted against testing temperatures.

Compressive creep experiments were further performed on Cu-Ta-Li and Cu-3at%Ta alloy. An ATS 2320 series lever arm creep tester with a 20:1 lever arm ratio was utilized for the experiments. A thermocouple was directly mounted on the sample to control the temperature during testing. A heating rate of 200° C hr^{-1} was applied in all testing conditions. Compression specimens were similar to quasi-statically tested samples, having a diameter and height of 3 mm each. The creep experiments were performed in air at 873 K (0.64 T_m) and 673 K (0.49 T_m), where T_m is the homologous temperature. Further, tests were conducted at 0.50 fraction of yield strength (at the respective temperatures) and for nearly 200 hours. All creep data was recorded including both elastic and plastic strain.

Note that for quasi-static and creep experiments, the testing was limited due to the time and resource-intensive nature of the experiments. As a result, statistical uncertainties and error bars have not been included; however, the observed statistical variation was found to be negligible.

Yield Strength from Microhardness Tests

The yield strength of Cu-Ta-Li and Cu-Ta alloys at elevated temperatures was obtained with microhardness measurements taken on the post-annealed samples. The yield stresses were obtained by using Tabor's rule ($\sigma_y = H_v/3$ where H_v is the Vickers microhardness).

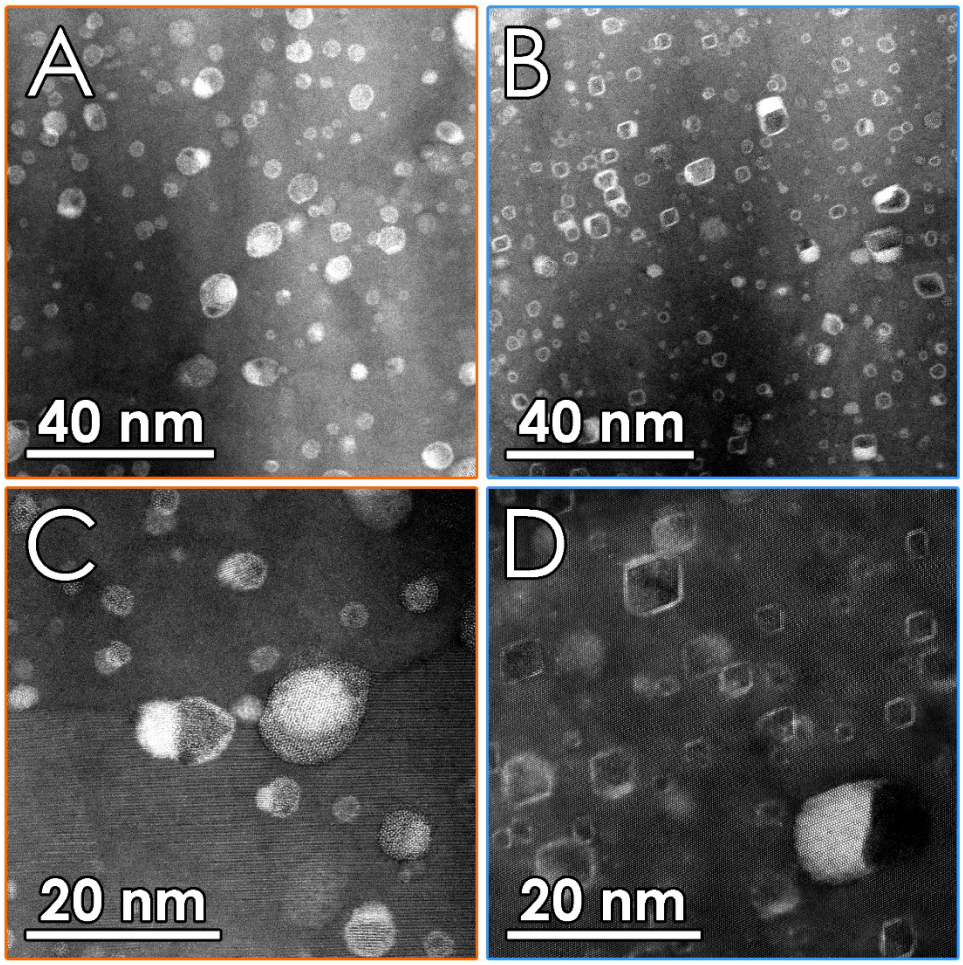

Fig. S1.

Aberration-corrected STEM high angle annular dark-field (HAADF) images at low and high magnification of (A,C) Cu-3Ta and (B,D) Cu-3Ta-0.5Li annealed at 900°C for 1 hour.

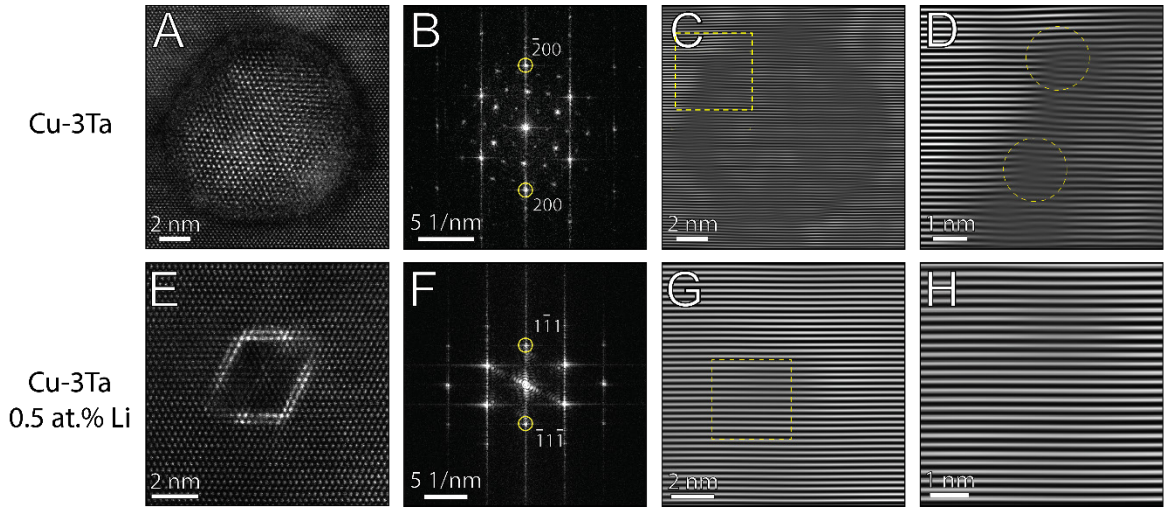

Fig. S2.

(A, E) STEM-HAADF images of nanoscale particles in binary Cu-3Ta and ternary Cu-3Ta 0.5Li annealed at 900 °C for 1hr, respectively. (B, F) Fast Fourier Transforms (FFTs) taken from the [110] crystallographic directions of the FCC matrix grains for both the binary and ternary alloy. (C, D, G, H) Filtered atomic-resolution images showing the presence of misfit dislocations surrounding the core-shell particle in (A) and the absence of dislocations surrounding the faceted particle in (E). Filtered images were constructed using the (200) and (1-11) reflections from the FFTs of the Cu-rich matrix in (A) and (E), respectively. The yellow dashed boxes in (C,G) denote the magnified regions in (D, H). Dashed yellow circles in (D) mark the location of dislocation cores.

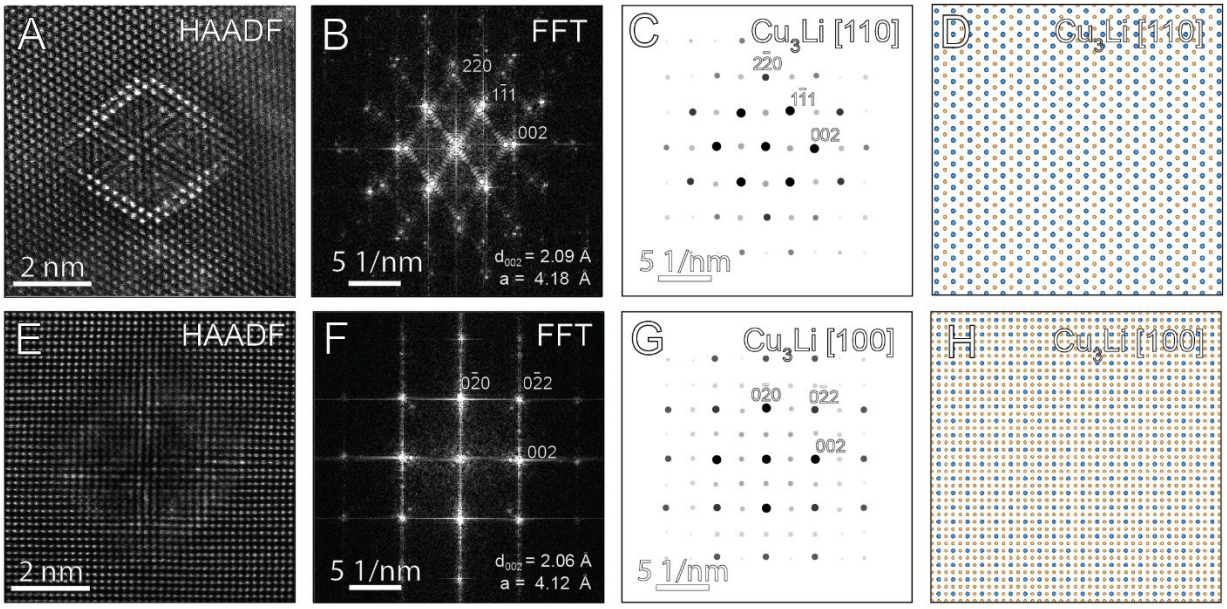

Fig. S3.

(A, E) STEM-HAADF images and corresponding (B, F) Fast Fourier Transforms (FFTs) taken from the [110] and [100] crystallographic directions of the FCC matrix grains in Cu-3Ta-0.5Li annealed at 900 °C for 1 hour. A coherent cube-on-cube crystallographic orientation relationship was observed between the FCC matrix grains and nanoscale particles. The experimental FFTs (B, F) are equivalent to simulated diffraction patterns from (C) the [110] and (G) the [100] crystal directions of cubic Cu_3Li, having the $L1_2$ structure, respectively. The grey refelctions in (C) and (G) are forbidden reflections. The STEM-HAADF images in (A, E) were also consistent with VESTA atomic structures corresponding with the (D) [110] and (H) [100] directions of Cu_3Li, where orange atoms denote Cu atoms and blue atoms denote Li atoms.

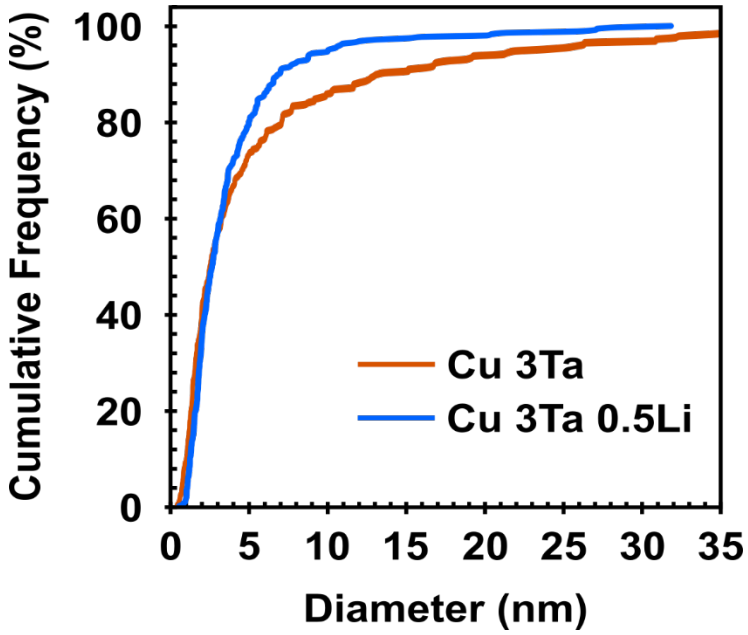

Fig. S4.

The plot of the cumulative distribution function for precipitate size in Cu-3Ta and Cu-3Ta-0.5Li alloys.

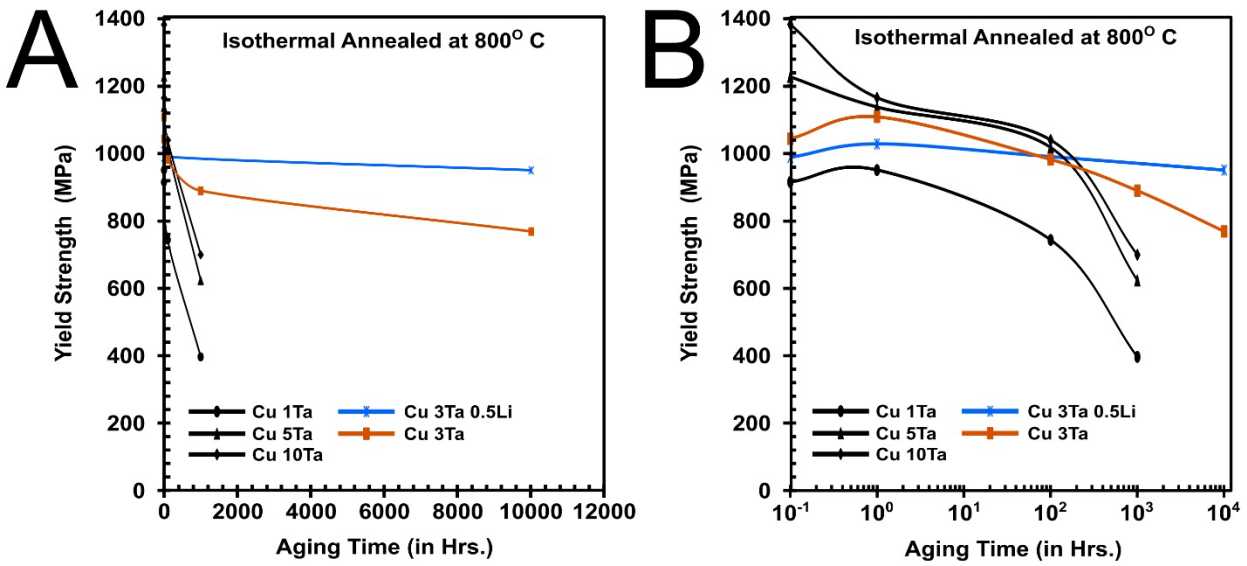

Fig. S5.

Yield strength for various compositions of binary Cu-Ta and Cu-3Ta-0.5Li plotted as a function of time at annealing temperatures of 800°C (0.8TM). (A) Linear scale, and (B) Logarithmic scale for the x-axis (time).

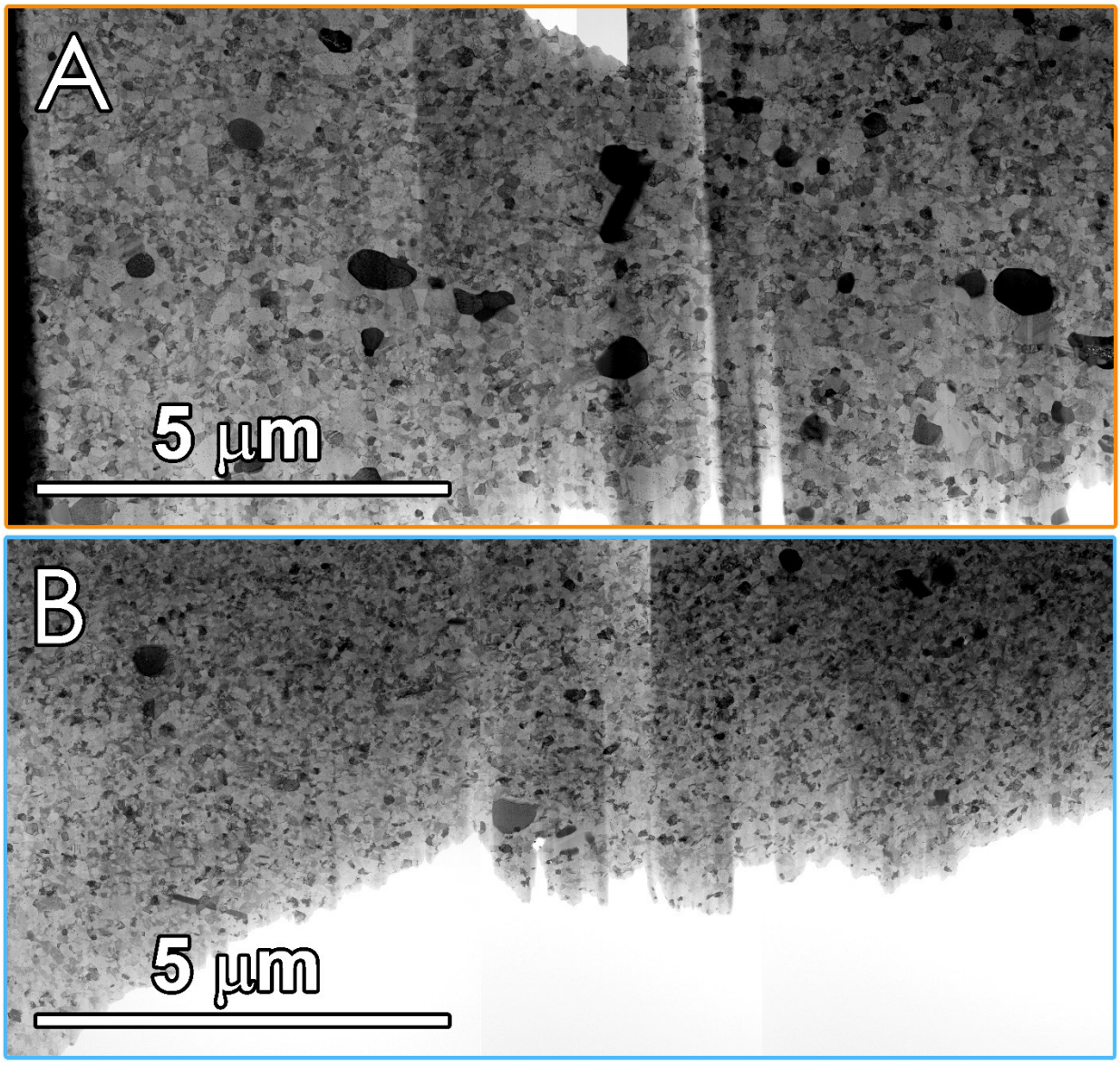

Fig. S6.

STEM bright-field composite images showing roughly 48 µm^2 of electron transparent area: after 10,000 hours of exposure to 800°C for (A) Cu–3Ta, and (B) Cu-3Ta-0.5Li highlighting the minimal coarsening occurring in the sample containing Li relative to the 3Ta.

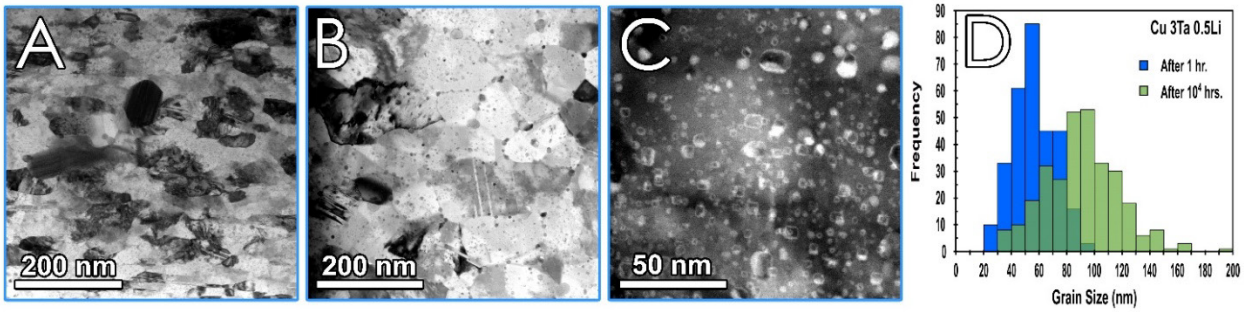

Fig. S7.

Medium magnification STEM bright field of Cu-3Ta-0.5Li after (A) 1 hour and (B) 10,000 hours at 800˚C ($0.8T_M$) highlighting the minimal grain growth. The change in the grain size was quantified to be a factor of 2 from 56 nm to 91 nm after the additional 9,999 hours of exposure. (C) STEM-HAADF image highlighting the retention and lack of coarsening of the cuboidal $L1_2$ structures after 10,000 hours of exposure. (D) Grain size distribution plot for Cu-3Ta-0.5Li after 1 and 10,000 hours exposure to 800˚C ($0.8T_M$).

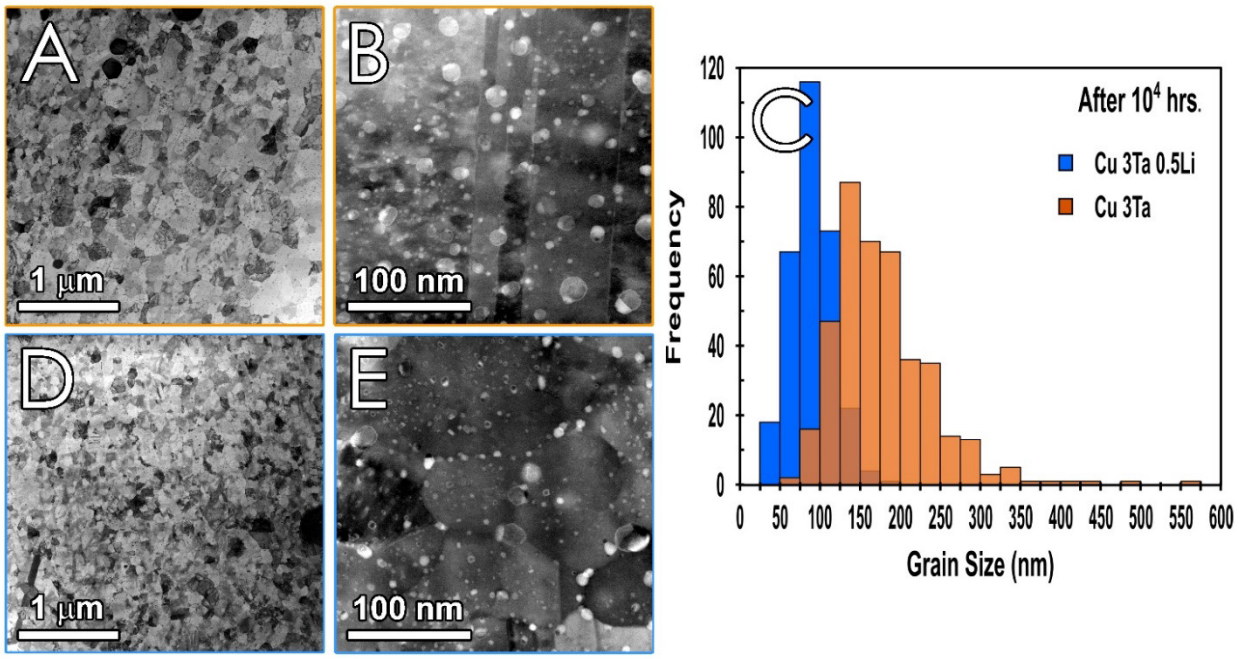

Fig. S8.

(A) and (D) Medium magnification STEM bright field of Cu-3Ta and Cu-3Ta-0.5Li respectively, (B) and (E) Higher magnification HAADF image of spherical and cuboidal clusters highlighting frequency and lack of coarsening after 10,000 hours at 800˚C respectively, and (C) grain size distribution plot for Cu–3Ta and Cu-3Ta-0.5Li respectively.

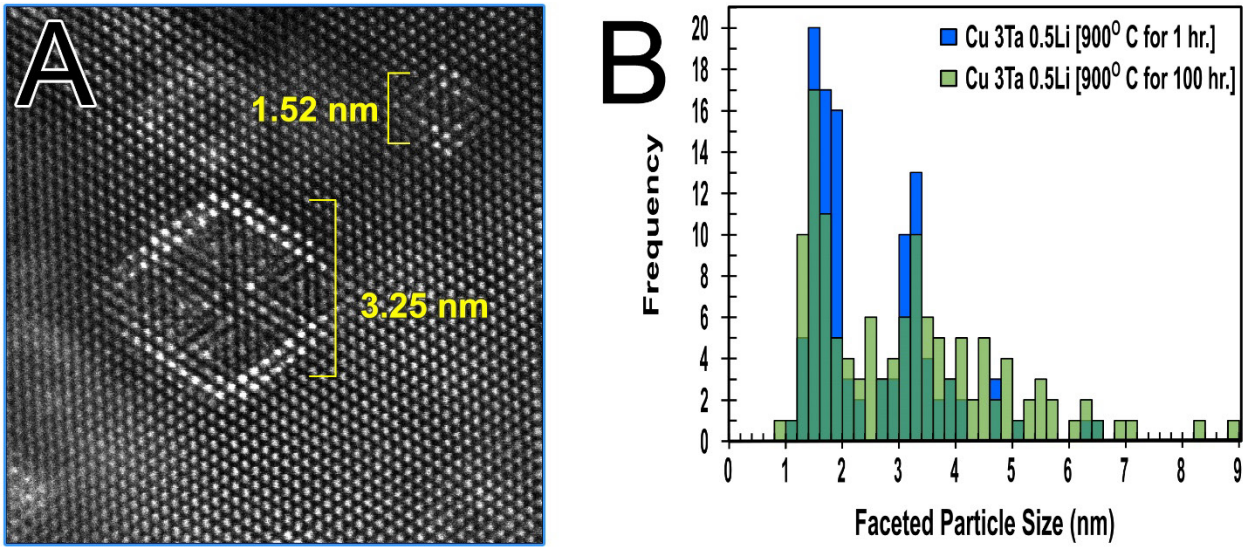

Fig. S9.

(A) Atomic-resolution ac-STEM HAADF image revealing discrete sizes of the $L1_2$ nanoclusters scaling at intervals of 1.6 nm. (B) Multi-modal distribution plot of $L1_2$ nanocluster sizes highlighting the propensity of sizes with peaks centering on 1.6, 3.2, 4.8, and 6.4 nm. Yellow brackets identify $L1_2$ nanoclusters of dimensions, 1.5 and 3.2 nm.

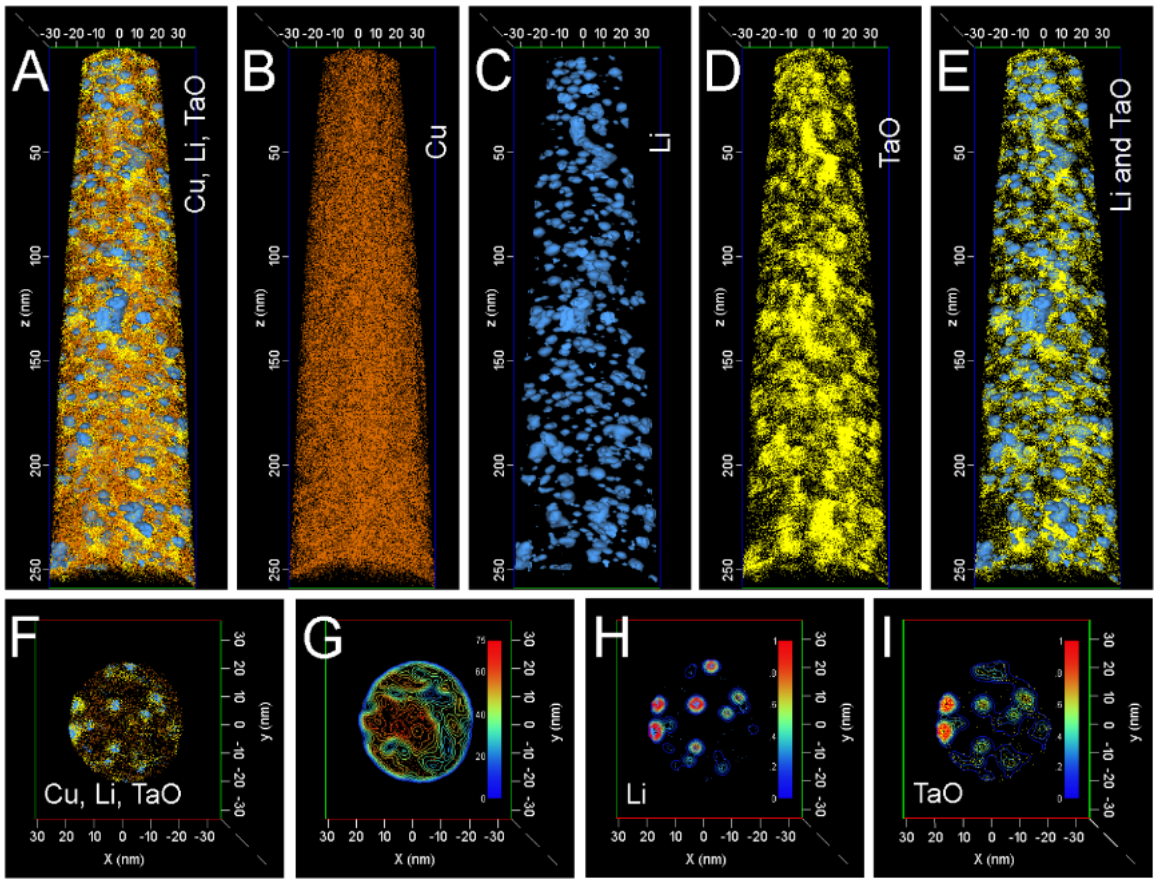

Fig. S10.

Atom probe analysis. (A) Atom map for Cu-3Ta0.5Li after 1 hour at 900˚C displaying both Cu and TaO atoms as well as Li isoconcentration surfaces set at 0.5 at.% Li for an entire tip. (B) Cu atom map. (C) 0.5 at.% Li isoconcentration surface present throughout the entire tip. (D) TaO atom map. (E) TaO atom map as well 0.5 at.% Li isoconcentration surface displayed. 10 nm thick 2-dimensional slice taken to display (F) Cu, Li, and TaO atoms. (G) Contour (density) map for Cu within the respective 2D slice. (H) Contour (density) map for Li within the respective 2D slice. (I) Contour (density) map for TaO within the respective 2D slice.

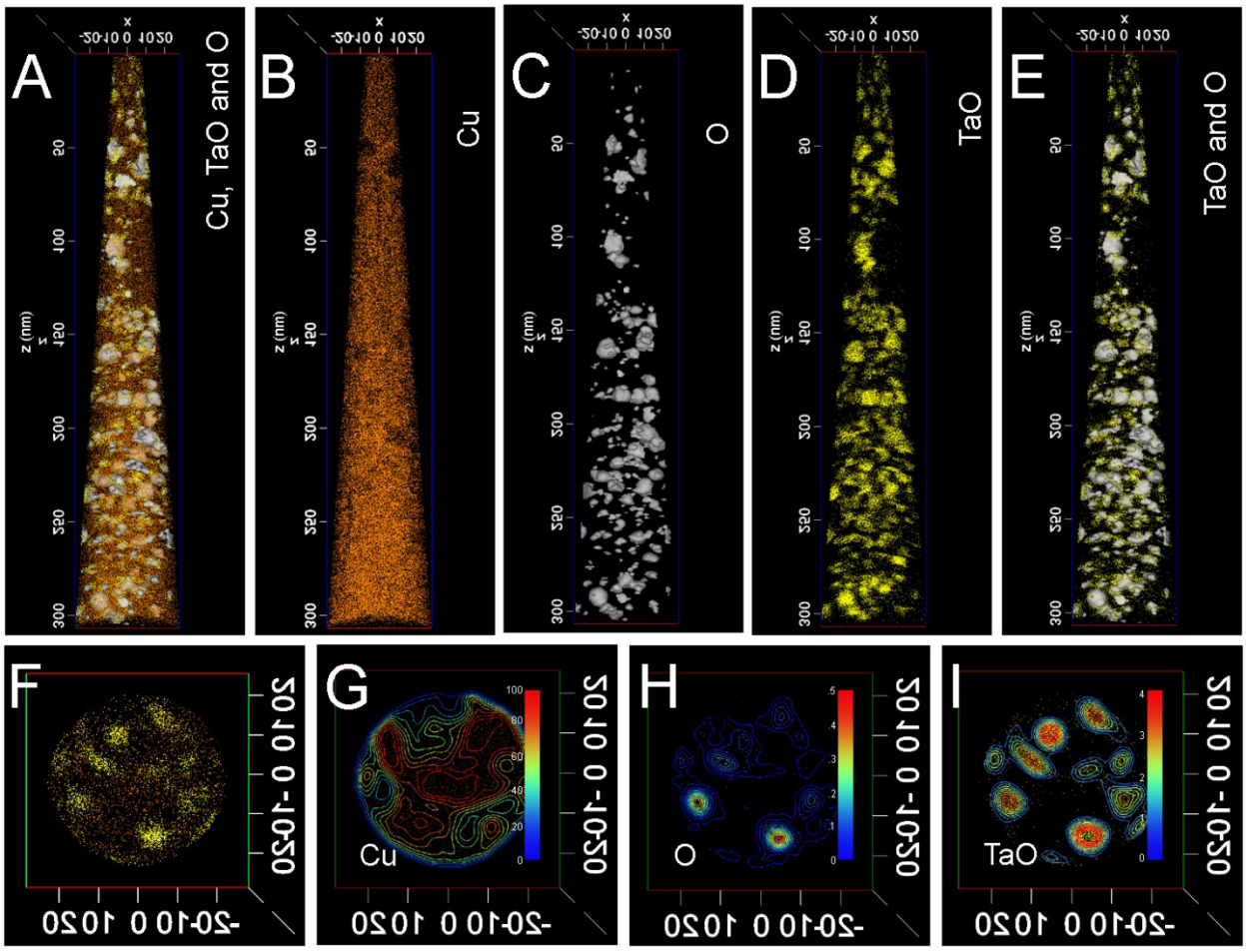

Fig. S11.

(A) Atom map for Cu-3Ta after 1 hour at 900˚C displaying both Cu and TaO atoms as well as O isoconcentration surfaces set at 3 at.% O for an entire tip. (B) Cu atom map. (C) 3 at.% O isoconcentration surface present throughout the entire tip. (D) TaO atom map. (E) TaO atom map as well 3 at.% O isoconcentration surface displayed. 10 nm thick 2-dimensional slice taken to display (F) Cu, TaO, and O atoms. (G) Contour (density) map for Cu within the respective 2D slice. (H) Contour (density) map for O within the respective 2D slice. (I) Contour (density) map for TaO within the respective 2D slice.

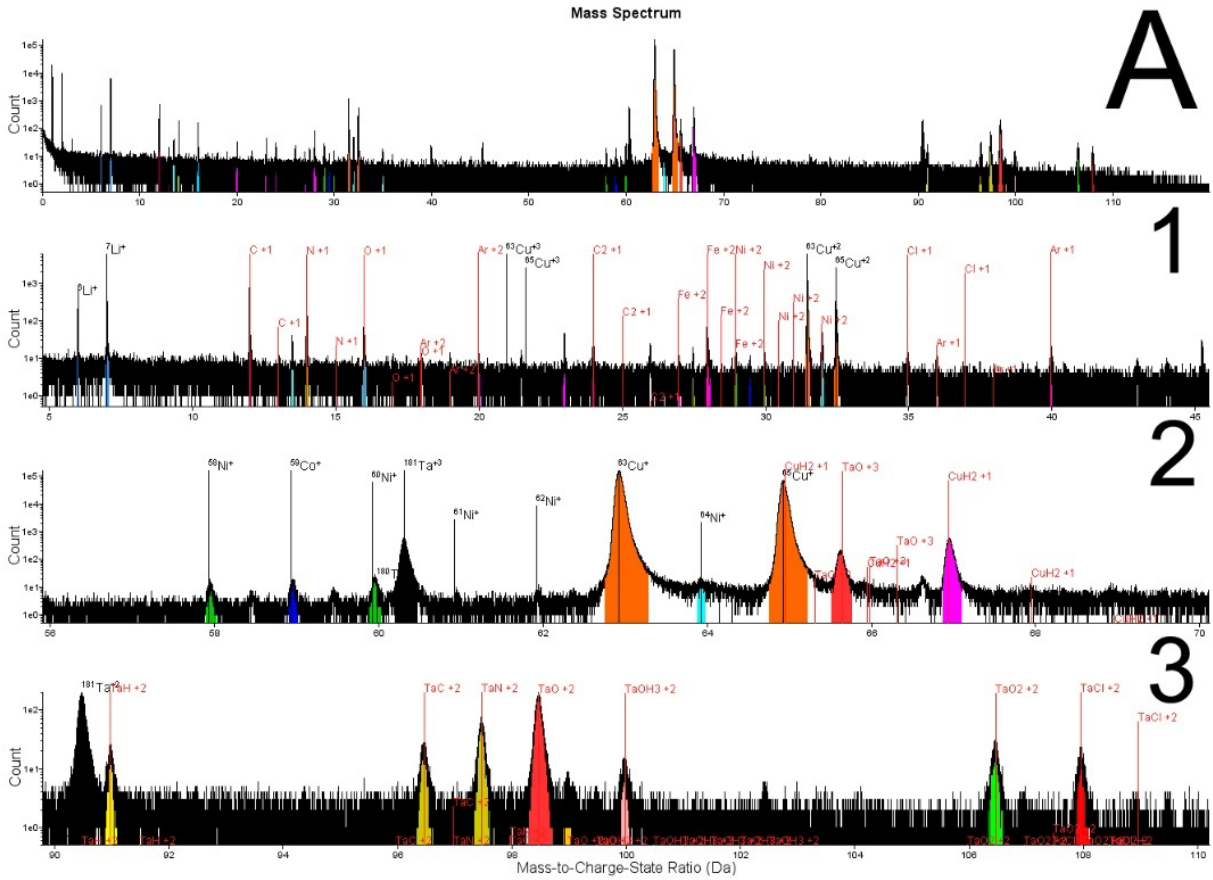

Fig. S12

(A) Full mass spectrum for Cu-3Ta-0.5Li after annealing at 900°C for 1 hour. The breakdown of regions labeled 1 through 3 covers the following ranges of the entire spectrum: 1) Da: 5-45; 2) Da:56-70; and 3) Da: 90-110.

Table S1.

Summary of lattice parameters and corresponding misfit measured between particle cores and the Cu-rich matrix in binary, Cu-3Ta, and ternary Cu-3Ta-0.5Li. Measurements were taken using the FFTs in Figure S7.

	Cu-rich Matrix	Particle Core	Misfit
Binary Cu-3Ta (Core-shell)	3.62 Å	4.44 Å	22.7 %
Ternary Cu-3Ta-0.5Li (Faceted)	3.64 Å	4.16 Å	14.3%

Table S2.

Summarizing the trend of stability of interface for different fractions of bilayer atoms replaced with Ta.

Interface Structure chosen	γ (J/m^2)	W (J/m^2)
$[110]_{precip.}$ ||$[110]_{matrix}Cu_3Li$, Cu with 100%Ta	1.11	3.33
$[110]_{precip.}$ ||$[110]_{matrix}$ Cu_3Li, Cu 0%Ta	4.76	1.11